

# Coexisting Flux Rope and Dipped Arcade Sections along One Solar Filament

Y. Guo<sup>1,2</sup>, B. Schmieder<sup>2</sup>, P. Démoulin<sup>2</sup>, T. Wiegelmann<sup>3</sup>, G. Aulanier<sup>2</sup>, T. Török<sup>2</sup>, and V. Bommier<sup>4</sup>

<sup>1</sup> *Department of Astronomy, Nanjing University, Nanjing 210093, China*

`guoyang@nju.edu.cn`

<sup>2</sup> *LESIA, Observatoire de Paris, CNRS, UPMC, Université Paris Diderot, 5 place Jules Janssen, 92190 Meudon, France*

<sup>3</sup> *Max-Planck-Institut für Sonnensystemforschung, Max-Planck-Strasse 2, 37191 Katlenburg-Lindau, Germany*

<sup>4</sup> *LERMA, Observatoire de Paris, CNRS, UPMC, Université Paris Diderot, 5 place Jules Janssen, 92190 Meudon, France*

## ABSTRACT

We compute the three-dimensional magnetic field of an active region in order to study the magnetic configuration of active region filaments. The nonlinear force-free field model is adopted to compute the magnetic field above the photosphere, where the vector magnetic field was observed by the *Télescope Héliographique pour l'Etude du Magnétisme et des Instabilités Solaires/Multi-Raies* (THEMIS/MTR) on 2005 May 27. We propose a new method to remove the 180° ambiguity of the transverse field. Next, we analyze the implications of the preprocessing of the data by minimizing the total force and torque in the observed vector fields. This step provides a consistent bottom boundary condition for the nonlinear force-free field model. Then, using the optimization method to compute the coronal field, we find a magnetic flux rope along the polarity inversion line. The magnetic flux rope aligns well with part of an H $\alpha$  filament, while the total distribution of the magnetic dips coincides with the whole H $\alpha$  filament. This implies that the magnetic field structure in one section of the filament is a flux rope, while the other is a sheared arcade. The arcade induced a left-bearing filament in the magnetic field of negative helicity, which is opposite to the chirality of barbs that a flux rope would induce in a magnetic field of the same helicity sign. The field strength in the center of the flux rope is about 700 gauss, and the twist of the field lines is  $\sim 1.4$  turns.

*Subject headings:* Sun: corona — Sun: filaments — Sun: magnetic fields — Sun: photosphere

## 1. Introduction

The magnetic field plays a key role in structuring the plasma in the corona, for instance in coronal loops and in filaments (or prominences).<sup>1</sup> Filaments have a dominant field component along their axis and are located above the inversion line of the radial component of the photospheric magnetic field, so in between two photospheric polarities. One traditionally distinguishes two types of magnetic configurations supporting filament material, according to the sign of the horizontal magnetic field component within the filament and orthogonal to it: if it is oriented such that it points from the positive to the negative photospheric polarity (located on both side of the inversion line), the configuration is called “normal”, otherwise it is “inverse”. Quadrupolar configurations can be either normal or inverse with respect to the central inversion line, depending on whether one refers to the outer or to the inner photospheric polarities, respectively.

Since filament plasma is typically a hundred times cooler and denser than the coronal surroundings (Tandberg-Hanssen 1995), while the observed velocities in prominences are much lower than the free-fall speed, a force is required to support the dense plasma against gravity. The Lorentz force can provide such stable support given that the plasma is located in magnetic dips. Dips are present in quadrupolar fields, or in bipolar fields that contain a flux rope, or at least highly sheared field lines located below a strong arcade field. The first model involving a quadrupolar field was derived by Kippenhahn & Schlüter (1957, see their sections 4,5), while Kuperus & Raadu (1974) first introduced a twisted flux tube. Both models have an inverse configuration. Indeed, it is relatively difficult to build a magnetic model with dips and a normal configuration, since deforming locally the top of an arcade by the gravity of dense plasma results in an unstable equilibrium (Kippenhahn & Schlüter 1957, their section 3). One possibility to create a dip in a bipolar force free field is to bend down the top of a very sheared arcade with the downward magnetic tension of a strong overlying arcade (Antiochos et al. 1994), but then the configuration still mostly comprises inverse polarity dips (Aulanier et al. 2002). More recently, Low & Zhang (2004) have obtained analytical solutions for both normal and inverse polarity configurations by solving the magneto-hydrostatic equations. For reviews of various prominence models, see, e.g., Démoulin (1998) and Mackay et al.

---

<sup>1</sup>Since “filament” and “prominence” refer to the same physical structure, seen on the solar disk and at the limb, respectively, we will use both terms alternately.

(2010).

Magnetic dips have been inferred from vector magnetic field observations in the photosphere (Lites 2005; López Ariste et al. 2006; Okamoto et al. 2008). Unfortunately, the observations cannot confirm if these dips are associated with a twisted flux tube or an arcade, because vector magnetic fields are currently not available for the chromosphere and the corona, although attempts to measure the magnetic fields above the photosphere have been made (Judge 1998; Lin et al. 2000; Liu & Lin 2008).

Therefore, coronal magnetic fields are usually extrapolated from the magnetic fields observed in the photosphere. Since the dynamic evolution of the corona is dominated by the Lorentz force, and since coronal structures like loops and prominences are observed to be stable over relatively long time periods, force-free equilibria are computed for this purpose. The MHD momentum equation then reduces to  $\mathbf{J} \times \mathbf{B} = 0$ , i.e. electric currents are parallel to the magnetic field. Using Ampère’s law,  $\mathbf{J} = (\nabla \times \mathbf{B})/\mu_0$ , where  $\mu_0$  is the permeability of the free space, the force-free field is expressed as  $\nabla \times \mathbf{B} = \alpha \mathbf{B}$ , where the force-free parameter  $\alpha$  is a function of space. If  $\alpha$  is permitted to vary over space, the resulting force-free field is nonlinear (NLFFF), whereas for constant  $\alpha$ ,  $\nabla \times \mathbf{B} = \alpha \mathbf{B}$  reduces to a linear equation, yielding a linear force-free field (LFFF). Setting  $\alpha = 0$  yields a potential field. Since the magnetic field is divergence-free,  $\nabla \cdot \mathbf{B} = 0$ ,  $\alpha$  is always constant along a given field line, i.e.  $\mathbf{B} \cdot \nabla \alpha = 0$ . NLFFF extrapolations require full vector magnetic fields as input at the boundary, whereas potential and LFFF extrapolations can be performed using merely the normal (line-of-sight) component of the magnetic field.

Three-dimensional (3D) magnetic configurations containing a flux rope have been constructed and discussed in detail using LFFF models (Aulanier & Démoulin 1998; Aulanier et al. 1998; Mackay et al. 1999) or linear magneto-hydrostatic models (Aulanier et al. 1999; Aulanier & Démoulin 2003; Dudík et al. 2008). Another approach is to insert locally a non force-free flux rope into an extrapolated potential field, then to relax the configuration with a magneto-frictional relaxation technique to a nonlinear force-free state (e.g. Mackay et al. 2000; Mackay & van Ballegooijen 2006, 2009). Applications of this flux rope insertion method can be found in, e.g., Bobra et al. (2008) and Su et al. (2009).

A more sophisticated approach is to use photospheric vector magnetograms as boundary conditions for the computation of nonlinear force-free fields in the corona, since, in active regions, in particular with complicated magnetic field structures, the force-free parameter  $\alpha$  usually changes in space (Régnier et al. 2002; Schrijver et al. 2005).

The presence of a flux rope in extrapolated coronal fields have been reported by several authors, who used different NLFFF extrapolation algorithms: Yan et al. (2001a,b) found a

flux rope with high twist of  $\sim 3$  turns and they studied its evolution before and after an X5.7 flare. Régnier & Amari (2004) found three flux rope systems in one active region with different twists of 0.5–0.6 turns for two cases and 1.1–1.2 turns in one case. Recently, Canou et al. (2009) have reported a flux rope in an emerging flux region with a twist of about one turn.

On the other hand, magnetic structures with dipped arcades have been reported in both quadrupolar and bipolar magnetic fields. There are two different types of quadrupolar magnetic arcades. One is the so-called FBP/FX arcade as labelled in Figure 3 of Aulanier & Démoulin (1998), and the other is the arcade in the so-called “wire model” (Martin et al. 1994; Martin 1998). The main difference between them is that an FBP/FX arcade is rooted in the main polarities, while an arcade in the wire model is rooted in the parasitic polarities. A highly sheared arcade in a bipolar field was modelled by Antiochos et al. (1994). The polarity of the filament field orientation is essentially inverse, however, there exist a few normal polarity dips as well in this model. That was briefly mentioned in Antiochos et al. (1994), and analyzed in details in Aulanier et al. (2002).

The question whether or not stable flux ropes are present in the corona is important not only for the magnetic structure of filaments and prominences, but also for the understanding of the initiation mechanisms of filament eruptions and coronal mass ejections (CMEs). Several theoretical CME models require the presence of a flux rope prior to, or at the onset of, an eruption (e.g., Forbes & Isenberg 1991; Török & Kliem 2005; Fan & Gibson 2007), whereas others assume that the preruptive configuration is that of an arcade, and that a flux rope is formed later on, during the eruption process (e.g., Antiochos et al. 1999; Moore et al. 2001).

Since NLFFF extrapolations require vector magnetic fields, a  $180^\circ$  uncertainty in the direction of the transverse field is always present (the so-called  $180^\circ$  ambiguity). This is due to the fact that opposite orientations of the transverse magnetic field generate the same linear polarization. In order to remove the ambiguity, some physical assumptions must be made. To this end, all commonly used algorithms minimize some physical quantities, such as the angle between the observed and modelled magnetic fields, the vertical gradient of the magnetic pressure, the vertical current density, some approximations to the total current density or the field’s divergence, or the combination of the quantities listed above (Metcalf et al. 2006, and references therein).

Another problem is that vector magnetograms measured by some instruments, such as THEMIS/MTR (*Télescope Héliographique pour l’Etude du Magnétisme et des Instabilités Solaires/Multi-Raies*), have a too small field of view (FOV) to fully cover large active regions, so that an imbalance of magnetic flux is often present. Even the self-consistent nonlinear

force-free solution proposed by Wheatland & Régnier (2009) suffers from this flux imbalance problem. In particular, the imbalanced flux reduces the absolute value of the force-free parameter  $\alpha$  in the regions where field lines connect outside the FOV of observed vector fields.

Finally, Metcalf et al. (2008) have shown that Lorentz forces and small-scale structures in the photosphere affect NLFFF extrapolations severely, while preprocessing, i.e. removing those forces and structures of the bottom boundary, improves the final result.

Due to the nonlinearity of the force-free equation, it is difficult to find analytical solutions for NLFFF, except for a class of axis-symmetric semi-analytical solutions derived by Low & Lou (1990). Therefore, several numerical methods have been developed, such as the Grad-Rubin, upward integration, MHD relaxation (magneto-frictional), optimization, and boundary element (Green’s function like) methods (Wiegelmann 2008, and references therein). In this study, we adopt the optimization method proposed by Wheatland et al. (2000) and implemented by Wiegelmann (2004). This method has been adopted to calculate the free energy evolution during flares (e.g., Guo et al. 2008; Jing et al. 2009).

Using the Low & Lou (1990) solution, Schrijver et al. (2006) have tested six NLFFF algorithms. They showed that the optimization method is able to recover the force-free field in the whole calculation volume if all the boundaries are specified, and to recover the lower inner region to a good degree if solely the bottom boundary is supplied. Furthermore, using the theoretical coronal flux rope models by Titov & Démoulin (1999) and Török & Kliem (2003), it has been recently shown that NLFFF extrapolation codes are capable of reconstructing significantly twisted flux ropes, as well as topological features of active region magnetic fields, with a high degree of accuracy (Valori et al. 2005; Wiegelmann et al. 2006a; Valori et al. 2010).

Here we extrapolate the coronal magnetic field in active region NOAA 10767, using the NLFFF optimization method, to construct the 3D magnetic configuration for a filament before its eruption. The vector magnetic fields are computed from observations obtained by THEMIS/MTR. The  $180^\circ$  ambiguity of the observed transverse fields is removed by adopting the principle that the fields change smoothly at the photosphere. We find a flux rope with a twist of  $\sim 1.4$  turns. The relationship between the magnetic fields and the filament is examined. We find that the flux rope only accounts for a part of the filament, while the total distribution of the magnetic dips coincides with the whole filament.

This paper is organized as follows: the observations, the method to remove the  $180^\circ$  ambiguity, and the preprocessing of the boundaries for the NLFFF extrapolation are described in § 2; The extrapolated magnetic fields and the flux rope are analyzed in § 3; The

discussion and conclusion are presented in § 4.

## 2. Observations and Data Analysis

### 2.1. Observations

Active region NOAA 10767 was observed by THEMIS/MTR from 9:54–10:41 UT on 2005 May 27. THEMIS (López Ariste et al. 2000; Bommier et al. 2007) is a French-Italian ground based telescope being operated on the Canary Islands of Spain. The telescope was designed to be instrumental polarization free because the polarization analyzer was put at the primary focus. THEMIS/MTR scanned the solar surface from east to west by a  $0.5'' \times 120''$  slit with a step size of  $0.8''$ . The Stokes profiles were observed for five spectral lines, however, only the profiles of the Fe 6302.5 Å and H $\alpha$  6562.8 Å lines were used in this study.

At each slit position, the two Stokes profiles  $I \pm S$  ( $S = Q, U$ , and  $V$ ) for each spectral line were recorded simultaneously on two different CCD cameras, for example  $(I + V)_{t1, \text{CCD1}}$  and  $(I - V)_{t1, \text{CCD2}}$ . The beam exchange technique was adopted, which means that within a short period  $\Delta t$ , the Stokes profiles  $I \mp S$  were recorded again, for example  $(I - V)_{t1 + \Delta t, \text{CCD1}}$  and  $(I + V)_{t1 + \Delta t, \text{CCD2}}$ . The beam exchange technique increases the polarimetric accuracy because it rules out the effects of the differences between the two channels of the beams. All the raw Stokes profiles were calibrated by the spectral de-stretching, dark current subtraction, and flat field correction (Bommier & Rayrole 2002; Bommier & Molodij 2002).

The  $I, Q, U$ , and  $V$  profiles were obtained by adding and subtracting the calibrated  $I \pm S$  profiles. We adopted the inversion code UNNOFIT (Landolfi & Landi Degl’Innocenti 1982; Bommier et al. 2007) to fit the Stokes profiles around the Fe 6302.5 Å line. UNNOFIT uses the Levenberg–Marquardt algorithm to make the least  $\chi^2$  fitting of the observed and modelled profiles, which are given by the Unno–Rachkovsky solution based on the Milne–Eddington approximation of the thermal structure of the solar atmosphere. We have compared the magnetic fields in a facula obtained by both UNNOFIT and MELANIE (Milne–Eddington Line Analysis using an Inversion Engine; Socas-Navarro 2001; Skumanich & Lites 1987), and found consistent results with the two inversion codes (Guo et al. 2010).

A part of the full disk magnetogram observed by MDI (Michelson Doppler Imager; Scherrer et al. 1995) in Figure 1a shows a larger FOV than that of THEMIS/MTR. We can see the surrounding magnetic environment out of the vector magnetic field observed by THEMIS/MTR, which is shown in Figure 1b. There is another active region in the northern hemisphere. Moreover, some positive polarities are present towards the east and south of the THEMIS/MTR observed region. This indicates that the observed vector magnetic field

does not cover an isolated region. The heliocentric angle in the center of the THEMIS/MTR FOV is about  $9^\circ$ . It is a good approximation to take the line-of-sight as the  $z$  axis of the extrapolation box.

## 2.2. The 180° Ambiguity Removal

We tried three different algorithms, namely the acute angle method, which compares the observed transverse field with a linear force-free modelled field (Wang et al. 2001), the non-potential magnetic field calculation method (Georgoulis 2005), and the iterative method developed by the group at University Hawai'i Institute for Astronomy (Canfield et al. 1993; Pevtsov et al. 1995; Leka & Skumanich 1999). However, none of them removed the ambiguity entirely. Each algorithm created some discontinuous borders separating two smooth solution domains, while there was no observational evidence showing that there existed such discontinuous borders. Moreover, the borders appeared at different places using the different algorithms, which indicates that the borders are created artificially, which is most probable due to the complexity of the active region. In particular, the transverse fields were highly sheared in the ambiguity-unresolved regions, where the assumptions of the three algorithms above are not adequate. The magnetic field obtained after removing the ambiguity by the non-potential magnetic field calculation method is shown in Figure 2a as an example. In Figure 2b, the absolute value of the force-free parameter  $|\alpha| = \mu_0 |J_z| / |B_z|$  is shown, where a small  $\epsilon_0 = 0.1$  gauss has been added to  $|B_z|$ , in order to avoid singularities. Large values of  $|\alpha|$  are located mainly along the inversion line of  $B_z$ , except for some values along the borders where transverse fields change abruptly.

In order to solve this problem, we have developed an interactive code, adopting the assumption that the magnetic fields change as smoothly as possible in the whole active region, which implies that the line-of-sight electric current density,  $|J_z|$ , has to be minimized in regions of abrupt changes of the transverse field. Our method is described in the following.

A map of  $|J_z|$  within the THEMIS/MTR FOV is displayed in Figure 3a. Firstly, we select a region which is enclosed by large  $|J_z|$  values where the transverse field changes abruptly (Figure 3b), and flip the vectors to the opposite direction. The result is displayed in Figure 3c. However, the vectors along the border of the selected region may still not change smoothly (see the oppositely directed transverse fields in Figure 3d). We therefore select sufficiently small boxes along the border, such as the box shown in Figure 3c, and zoom in as shown in Figure 3d. Now we can select a region that contains only tens of points, and define a local direction denoted by the larger arrow in Figure 3d. The transverse field vector will be flipped to the opposite direction if it makes an obtuse angle with the defined

direction. The result is shown in Figure 3e. Secondly, the steps shown in Figure 3c-e are repeated along the border that encloses the gray-scale reversed (dark) region in Figure 3b, until all the transverse field vectors along the border change smoothly. Finally, the steps shown in Figure 3b–e are repeated, until all the transverse fields in the regions of abruptly changing vectors enclosed by large  $|J_z|$  are flipped. The final map of  $|J_z|$ , where all these large currents are removed, is displayed in Figure 3f.

We apply the above procedure to the magnetic field for which the ambiguity has been preliminarily removed by the non-potential field calculation method (Figure 2a). The  $180^\circ$  ambiguity removal of this active region is highly improved by our method, since the transverse field vectors change more smoothly (Figure 2c). Still, there remain some regions of relatively large currents, which cannot be removed by our method. This seems plausible, since the spatially partly unresolved magnetic field evolved while THEMIS/MTR scanned this very dynamic active region. Furthermore, it is possible that there were indeed abruptly changing transverse fields in the true magnetic configuration.

### 2.3. Preprocessing of the Boundary Data

In the NLFFF model, the boundary condition is necessarily force-free and torque-free in a well isolated region, for which all field lines are closed within the model domain (Aly 1989). But these criteria are usually not satisfied in real data, because the observed magnetic field is not well isolated, and because the field in the photosphere is not force-free. This implies that the extrapolation results depend on how the uncompensated magnetic flux connects with the flux outside of the observed field region, i.e. the reconstruction problem does not have a unique solution (Wiegmann et al. 2006b). In principle, the force-free and torque-free integrals are exactly valid for the force-free field, if taken over the entire boundary surface of any volume (for example, all six boundaries of a rectangular box). However, because the lateral and top boundaries are a priori unknown, we have to rely on the assumption that the effects of these unknown boundaries are small enough to be ignored, which requires that the bottom boundary is well isolated and flux balanced.

In order to simulate a force-free boundary on the bottom layer, we adopt the preprocessing routine developed by Wiegmann et al. (2006b), which minimizes the total force and torque. It also smoothes the magnetic fields observed in the photosphere, while it requires that the fields only change within the measurement accuracy. Considering that the circular polarization is measured more precisely than the linear one, the preprocessing of the line-of-sight magnetic fields  $B_z$  is only modified by the smoothing in a local area of  $5 \times 5$  grid points for the case studied here. The force-free and torque-free conditions, as well as

the smoothing are used to preprocess the transverse fields  $B_x$  and  $B_y$ . We suppose here that the force and torque outside the observation’s FOV have much smaller contributions than the ones inside it. Although the force-free and torque-free terms are global, the terms constraining the preprocessed data within the observation accuracy and the smoothing term guarantee that the preprocessing on  $B_x$  and  $B_y$  has a local behavior.

Observationally, however, the bottom boundary is not always guaranteed to be isolated from other active regions and the magnetic flux is not always balanced. This is because accurate vector magnetic field measurements require a high spectral resolution, which is a burden that limits the spatial and temporal resolution, as well as the FOV. In order to enlarge the FOV, so to enclose an isolated bottom boundary, one could embed the vector magnetic field into larger FOV observations, such as line-of-sight magnetic fields observed by MDI. But this would yield an inconsistent boundary for a nonlinear force-free model, since the line-of-sight fields do not contain any currents to provide the information for the correct field line connections (DeRosa et al. 2009). Alternatively, one could cut out a smaller flux balanced FOV from the vector data and use it as the bottom boundary. But this would not solve the problem either, since the flux balance is a necessary condition for a well isolated magnetic field, but not a sufficient one. In doing so, one would lose more further field line connections, and the side boundaries would affect the inner region more. For these reasons, we decided to apply the preprocessing to the magnetic fields within the full FOV of THEMIS/MTR.

### 3. Results

The preprocessed bottom boundary is submitted to the optimization code to perform the NLFFF extrapolation. The principle of the method is to minimize the objective function,

$$L = \int_V \omega(x, y, z) [B^{-2} |(\nabla \times \mathbf{B}) \times \mathbf{B}|^2 + |\nabla \cdot \mathbf{B}|^2] dV, \quad (1)$$

where  $\omega(x, y, z)$  is the weighting function (Wheatland et al. 2000; Wiegelmann 2004). The 3D magnetic field is computed in a box of  $529 \times 260 \times 260$  grid points in the Cartesian coordinates with a uniform cubic grid, where  $\Delta x = \Delta y = \Delta z \approx 330$  km is the spatial resolution. We have checked the convergence of the code, which has reached a steady state that defined as  $\frac{\partial L}{\partial t}/L < 1.0 \times 10^{-4}$  for 100 consecutive iteration steps.

Selected field lines of the extrapolated region are plotted in Figure 4a. The red field lines outline the main connectivity. We find a flux rope oriented along the polarity inversion line in the center of the FOV (shown by field lines in different colors). Different views on the flux

rope are displayed in Figure 4b-d. Orange field lines outline the sheared arcade overlying the flux rope. The field lines become increasingly less sheared with respect to the inversion line with height above the bottom boundary. We estimate the twist in the flux rope to be  $\sim 1.4$  turns. The height of the apex of the highest rope field lines above the bottom boundary is about 1500 km. We have tested the extrapolation with higher grid resolutions in  $z$ -direction, where  $\Delta z = \Delta x/2 = \Delta y/2$  and  $\Delta z = \Delta x/4 = \Delta y/4$ . The twisted field lines are recovered in both cases, however, the codes with different spatial resolutions do not reconstruct the flux rope up to the same physical height, but to almost the same number of grid points. It is currently not clear to us what causes this numerical effect, which requires further study. However, the facts that the code finds twisted field lines for all three resolutions, and that the vector data show bald patches along the polarity inversion line at their location (see below), strongly supports the realness of the flux rope.

Magnetic dips re present in the extrapolated flux rope. Dips along the magnetic field lines are defined by  $\mathbf{B} \cdot \nabla B_z > 0$  and  $B_z = 0$ . Bald patches are dips which are tangential to the photosphere. They define separatrices where current sheets are typically present (Titov et al. 1993). Bald patches can be recognized from the  $180^\circ$  ambiguity removed vector magnetic field map in Figure 2c: they are located where the transverse fields have a component normal to the inversion line, pointing from the negative polarity to the positive one. Some bald patches are also visible in Figure 4c,d: they are located where the red, dark blue, and green field lines are tangential to the bottom layer (more precisely, since the boundary data have some noise, the integration of the field lines starts from a point slightly above the inversion line,  $\approx 1/10$  of the mesh size).

In the following subsections we check the degree of force-freeness and divergence-freeness of the extrapolated magnetic field. Then, we study the relationship between the flux rope and the filament as observed in  $H\alpha$ . Finally, we provide additional evidence for the existence of the flux rope.

### 3.1. The Force-Free and Divergence-Free State

We now test whether the magnetic field has reached a truly force-free state. The current-weighted average of the sine of the angle between the current density and the magnetic field is used as the force-free state metric (Wheatland et al. 2000):

$$\langle \text{CW sin } \theta \rangle = \frac{\sum_i J_i \sin \theta_i}{\sum_i J_i}, \quad (2)$$

where

$$\sin \theta_i = \frac{|\mathbf{J}_i \times \mathbf{B}_i|}{J_i B_i}. \quad (3)$$

The summation is realized within the subdomain shown in Figure 5a, which spans over  $80 \times 80 \times 5$  grid points labelled with the index  $i$ . For a perfectly force-free field, the current density and the magnetic field are parallel to each other at each grid point, i.e.  $\langle \text{CW} \sin \theta \rangle = 0$ . In Table 1, we list  $\langle \text{CW} \sin \theta \rangle$  for different bottom boundary conditions of the extrapolation (see below). For the extrapolation discussed in the previous subsection,  $\langle \text{CW} \sin \theta \rangle = 0.28$ , which corresponds to an angle of  $\sim 16^\circ$ . We plot  $\sin \theta_i$  at the bottom layer and the electric current density around the flux rope in Figure 5. Typically,  $\sin \theta_i$  is smaller where  $J_i$  is larger, and the large values of  $J_i$  usually appear along the flux rope. We select 60 points inside the flux rope and compute  $\langle \text{CW} \sin \theta \rangle$ , which is 0.09 implying an relatively small angle of  $\sim 5^\circ$ .

Another metric for the extrapolation result is the degree of divergence-freeness of the magnetic field. To this end, the unsigned average of the fractional flux change,  $\langle |f_i| \rangle$ , is calculated, where  $|f_i| = |(\nabla \cdot \mathbf{B})_i| / (6B_i / \Delta x)$ . For the extrapolation discussed above,  $\langle |f_i| \rangle$  is about  $4.9 \times 10^{-3}$  in the selected volume (Table 1). For comparison,  $\langle |f_i| \rangle$  is  $4.8 \times 10^{-5}$  for the Low & Lou field calculation, averaged over all grid points of the extrapolation domain (Wheatland et al. 2000), and it is  $5.0 \times 10^{-4}$  for the extrapolation of preprocessed and smoothed photospheric data generated by the flux rope insertion method (van Ballegoijen et al. 2000; van Ballegoijen 2004), using the optimization method (Metcalf et al. 2008).

In order to test which is the best way to choose and preprocess the bottom boundaries, we have made two more extrapolations and calculated their force-free and divergence-free metrics (see Table 1). In the first case, the vector magnetic fields observed by THEMIS/MTR are embedded in an MDI magnetogram (Figure 1a). The transverse components outside the rectangle are adopted by a potential field extrapolation using the line-of-sight magnetic fields obtained by MDI in the FOV shown in Figure 1a. We define the flux balance parameter,  $\epsilon_f$ , as

$$\epsilon_f = \frac{\sum_i (B_z)_i \, dS}{\sum_i |(B_z)_i| \, dS}. \quad (4)$$

Then,  $\epsilon_f$  is 0.02 for the combined magnetogram, which is much better than  $\epsilon_f = -0.47$  for the FOV of THEMIS/MTR only. After that, the preprocessing and smoothing is applied to this flux balanced bottom boundary, and the preprocessed vector magnetic field within the FOV of THEMIS/MTR is used as the boundary conditions for the extrapolation. In the second case, the vector magnetic fields observed by THEMIS/MTR are neither embedded in an MDI magnetogram, nor preprocessed, i.e. used directly as boundary conditions.

From Table 1, we can see that the force-free measure of the magnetic field extrapolated

with the embedded, flux balanced boundary is worse than for the boundary preprocessed and smoothed full FOV of THEMIS/MTR. This indicates that embedding the vector magnetic field into an inconsistent larger FOV decreases the quality of the extrapolation in our case. The preprocessing and smoothing helps the extrapolation to converge to a force-free state in both cases. If the magnetic field is not preprocessed, the extrapolated field does not vary much from the potential field ( $E/E_{\text{pot}} = 1.01$  is very small), and  $\langle \text{CW} \sin \theta \rangle = 0.68$  is relatively large (see Table 1). We cannot recover the flux rope any more in this case. The preprocessing and smoothing is therefore crucial for the successful NLFFF extrapolation from the photospheric vector magnetic fields in our case. The divergence-free measure always keeps at the accuracy of the magnetic field measurements for all three cases.

### 3.2. Comparison Between the Magnetic Field and the H $\alpha$ Filament

The H $\alpha$  line center image observed by THEMIS/MTR in Figure 6a shows the filament at the location where we find the flux rope. Towards the south-west, an arch filament system is present, indicating the emergence of new magnetic fields from the convective zone. We overlay the extrapolated field with the H $\alpha$  image in Figure 6b. The accuracy of the alignment can be guaranteed below one pixel, since the spectra of Fe 6302.5 Å and H $\alpha$  6562.8 Å were recorded by THEMIS/MTR simultaneously. The images constructed by these two lines mismatch each other only because of their slightly different pixel sizes. This is corrected by interpolation of the H $\alpha$  image to the spatial resolution of the magnetic field map. From Figure 6b, we can see that the flux rope aligns with the filament very well. However, it accounts only for a part of the filament.

We calculate the magnetic dips, using a horizontal/vertical grid size of  $\sim 330$  km, and overlay them with the H $\alpha$  line center image, as shown in Figure 6c–e. The field lines starting from the dips are integrated in both directions up to a filling height of 300 km, or, to a local maximum if the field line starts to descend before it reaches this height. It can be seen that the locations of the dips are very well aligned with the filament over all its length. The western part of the filament does not coincide with the flux rope, but with the dips along the sheared field lines. The transverse field at these dips has a component orthogonal to the spine of the filament, pointing from positive to negative  $B_z$ , i.e. the field has normal polarity. In the eastern part of the dip distribution area, along the flux rope, the field has inverse polarity. So, there are both normal polarity and inverse polarity magnetic structures supporting different parts of one filament.

A two-dimensional (2D) section in the western part of the region ( $x \in [-60.0, -50.0]$  arcsec,  $y = -114.7$  arcsec, and  $z \in [0.0, 1.0]$  arcsec) is selected, and the field lines are integrated

from some sample points on this section. The field lines are plotted in Figure 6f and they span over a quadrupolar region. Figure 6g reveals that the dips along the arcade field lines, at  $x = -56.7$  arcsec and  $x = -52.0$  arcsec, have a bald patch and X-point below them when they are viewed in 2D, respectively. They corresponds to the so-called FBP and FX configuration as labelled in Figure 3 of Aulanier & Démoulin (1998). In a quadrupolar magnetic field, the notion of normal/inverse polarity depends on which reference polarities are used. If we use the parasitic polarity below the local dip, an FBP configuration is inverse. Or, if we use the main polarities where the entire field line is rooted, the FBP configuration is normal. We prefer the latter definition. For the sheared field lines (not in quadrupolar magnetic fields), the configuration is preferentially normal. These sheared arcade with normal polarities could partly be associated with the model in Antiochos et al. (1994), even though the latter incorporates a majority of inverse polarity dips.

It is also worth to note that the dips are located not only along the main body of the filament, but also at lateral extensions, called feet or barbs (located around  $[x, y] = [-90, -125]$  arcsec and  $[-60, -100]$  arcsec in Figure 6c, in the arcade part of the filament). The organization of the barbs implies a left-bearing filament, which is defined as follows. Viewed from either side of the filament, the barbs on the side closer to the observer veer from the filament axis to the left (Martin et al. 1994; Martin 1998). Such lateral extensions were previously associated with small polarities having the opposite field sign to the dominant polarity on both sides of the filament (Aulanier & Démoulin 1998; Aulanier et al. 1999). Recently, Mackay & van Ballegooijen (2009) found such lateral dip extensions in a NLFFF model with small magnetic polarities of both sign. In our case, the polarities are not small, rather the lateral dip extensions appear where the photospheric inversion line is strongly bent (Figure 6a). Another difference to earlier models is that the lateral dip extensions are not due to the deformation of a twisted flux tube, but are present in an arcade (Figure 6f). This implies that these lateral dips have a normal (rather than inverse) configuration (just as the part of the filament between these lateral extensions).

We do not find dips in the area above  $[x, y] \approx [-95, -115]$  arcsec, although filament material is located there. Several reasons may account for this. Firstly, we find large currents in this region as shown in Figure 5. The fields do not change continuously in some places, therefore the force-free field extrapolation may not recover the result accurately enough in this region. Secondly, from Figure 4c, we can see that the western foot of the flux rope becomes vertical. Then dips cannot be found although the field lines are still twisted there. Thirdly, the field lines are only integrated up to the filling height of 300 km, which is empirical, while the plasma could flow away along the field lines. This may also explain the gap between dip distribution and the filament material. Finally, the NLFFF model does not consider gravity and thermal pressure gradients, which may alter the distribution of the

magnetic dips, since the gravity can locally amplify the depth of the dips, and induce new ones in the surrounding field. It is also worth to note that the filament does not follow the polarity inversion line, and passes on the north side of it in this area where we do not find dips.

The local magnetic helicity in our studied region is negative, as apparent from the left-handed flux rope and the left-skewed overlying arcades (an arcade is left-skewed if it bears an acute angle anticlockwise from the associated polarity inversion line when viewed from the top). Furthermore, the filament chirality as inferred from the extrapolated magnetic field is dextral, since the axial field component along the whole filament points to the right when viewed from the positive magnetic polarity region. Note that this “axial field chirality” (dextral/sinistral) is different from the “barb chirality” (left-bearing/right bearing) as defined above. In order to obtain the latter also for regions where no barbs are present, or are not visible due to the limited resolution of the  $H\alpha$  image, we use the orientation of the field line segments around the dips (shown in red in Figure 6c) as a proxy. It can be seen from the figure that the “barbs” are right-bearing (resp. left-bearing) in the flux rope (resp. arcade) part of the extrapolated field along the filament. Finally, as mentioned above, we find inverse (resp. normal) configuration in the flux rope (resp. arcade) dips in the field. These findings are summarized, and compared with the predictions of the arcade-type wire model for filaments (Martin et al. 1994; Martin 1998) in Table 2.

It is found that in the observed filament, both sections have opposite barb chiralities for the same axial field chirality (due to inverse vs. normal magnetic field orientations within the dips), and that neither section is consistent with the properties of the wire model all together (since this model does not incorporate dips, and it requires an opposite helicity sign in the filament fields).

### 3.3. Magnetic Fields in the Flux Rope

In order to confirm the existence of the flux rope, we decompose the magnetic field components in a flux rope reference frame and study the distributions of these components. The most important issue of the decomposition is to determine the axis of the flux rope. Two assumptions are made: the flux rope between points 1 and 3 in Figure 7a is oriented horizontal and tangent to the inversion line. Then, we fit the inversion line between points 1 and 3 by a third order polynomial, shown by the solid curve in Figure 7a. Point 2 is used as an example to show how the flux rope reference frame is defined. As shown in Figure 7a,  $p$ - and  $v$ -directions are tangential and orthogonal to the fitted inversion line at point 2, respectively. The directions at points 1 and 3 can be defined similarly.

We decompose the magnetic field into  $p$ -,  $v$ -, and  $z$ -direction components as shown in Figure 7a, and plot their distributions along the height ( $z$ -direction) at point 2 in Figure 7b. The distributions of  $B_p$ ,  $B_v$ , and  $B_z$  at points 1 and 3 are very similar to that at point 2. The component parallel to the flux rope,  $B_p$ , increases first with height until the axis of the flux rope, then it decreases. The strength of  $B_p$  on the axis is  $\sim 700$ – $800$  gauss, which is almost equal to the total field strength  $B$ , because  $B_v$  and  $B_z$  are close to zero there. At any height,  $B_p$  is larger than  $B_v$  and much larger than  $B_z$ , showing that the flux rope is almost horizontal and not very strongly twisted along the inversion line.  $B_v$  changes its sign when it crosses the axis of the flux rope, which is a clear evidence that the field lines rotate around the axis.  $B_z$  is always close to zero because the magnetic field is almost horizontal at the sample point. The originally observed magnetic fields on the bottom boundary (before preprocessing) are also shown as larger symbols in Figure 7b. The largest difference is  $\sim 25\%$  for the  $B_p$  component.

The increase of the magnetic field strength from the edge to the center of the magnetic flux rope is a simple consequence of the force balance, as follows. The Lorentz force can be written as

$$\mathbf{J} \times \mathbf{B} = \frac{1}{\mu}(\mathbf{B} \cdot \nabla)\mathbf{B} - \nabla \left( \frac{B^2}{2\mu} \right). \quad (5)$$

In the force-free equilibrium state, namely  $\mathbf{J} \times \mathbf{B} = 0$ , the magnetic tension compensates the gradient of the magnetic pressure such as

$$\frac{B^2}{R} - \frac{\partial(B^2/2)}{\partial n} = 0, \quad (6)$$

where  $\mathbf{B} = B\mathbf{t}$ , and  $\mathbf{t}$  is tangential to the field line. The normal unit vector  $\mathbf{n}$  is defined as  $\mathbf{n}/R = d\mathbf{t}/ds$ , where  $R$  and  $s$  are the radius of curvature and the arc length along the field line, respectively. For the flux rope,  $B^2/R$  is a nonzero positive number, hence, the strength of the magnetic field must increase from edge to the center to compensate the magnetic tension.

#### 4. Discussion and Conclusion

The computation of the coronal field from vector magnetic fields is still in the development stage, in particular in trying to obtain high temporal, spatial, and spectral observations, as well as removing the intrinsic  $180^\circ$  ambiguity. Regarding the NLFFF extrapolation itself, better algorithms to treat the problem and new methods to get consistent boundary conditions are still under discussion. We have made advances on two main steps of the process.

Firstly, we have tested three methods to remove the  $180^\circ$  ambiguity. Since none of the results was fully satisfactory, because discontinuities in the field orientation were always present, we have developed a new method which succeeds to provide a coherent orientation of the magnetic field through all the magnetogram, except for some small regions where abrupt changes of the transverse field could not be fully removed (see Section 2.2). This step is fundamental for a successful extrapolation.

Secondly, the vector magnetograms measured by THEMIS/MTR often have a too small FOV to include all the magnetic field related to an active region. This field of view limitation is also present with some other vector magnetographs. This implies a non-negligible imbalance of magnetic flux in many cases. For the analyzed active region, we show that embedding the vector magnetogram in a larger line-of-sight magnetogram to resolve the flux imbalance introduces inconsistencies in the computed field (since the line-of-sight field has no information on electric currents). We found that it is better to do the preprocessing of the data on the original FOV of the vector magnetogram. In particular, the metrics used to test the results are best in this case (Table 1).

Our extrapolation results show that the field lines connecting to areas outside the box mostly originate from the negative polarity, and that field lines from this polarity do not connect to the region where we found the flux rope (Figure 4a). The size of the flux rope is relatively small compared to the FOV of THEMIS/MTR. The rope lies in the center and all its field lines are closed within the FOV. All these factors prevent the flux rope from being significantly affected by the flux imbalance of the bottom boundary.

To further test our results we compute the magnetic dips. When viewed from above, their spatial distribution superposes well with the observed  $H\alpha$  filament (Figure 6c). The dips of the flux rope reproduce the thin part of the filament (its eastern part), while dips in arcade field lines describe very well the broad lateral extent of the filament’s western part. This is a successful test of our extrapolation, and it also confirms that  $H\alpha$  filaments are supported in magnetic dips.

The studied filament has a complex magnetic structure, formed partly by a flux rope and partly by a dipped arcade, and it is located above a very bent (S-shaped) inversion line. This strong bending has similar effects as small parasitic polarities located in the corridor of other filaments, as it also induces the creation of lateral extensions of dips. We found that these extended dips correspond to the feet, or barbs, of the  $H\alpha$  filament (Figure 6c). Since these lateral extensions are located in dipped arcades, their chirality is opposite to the one present in a flux rope. More precisely, in the analyzed configuration the magnetic helicity is negative and the lateral extensions are left-bearing, while they should be right-bearing in a flux rope configuration (as shown in previous studies). We cannot test this for the studied

filament, since no lateral extensions are present in the region of the flux rope. However, we can already see that, in a magnetic field with the same helicity, the chirality of the pattern arranged by the field line segments around the dips in the flux rope is right-bearing, and that of the arcade is left-bearing (Figure 6c,f). Therefore, flux ropes and arcades preferentially induce opposite chirality for the filament barbs and feet in the magnetic field with the same helicity.

However, it was generally assumed that the magnetic structure of a filament is either that of an arcade or that of a flux rope. Therefore, if one observes opposite barb chiralities in different parts of one filament, one might wrongly conclude that the magnetic field has also opposite helicity in these parts. In some cases where both right-bearing and left-bearing barbs are found for one filament (e.g., Chandra et al. 2010), the helicity sign for the associated magnetic field may be the same, while one part of the filament is supported by a flux tube, and the other by an arcade.

Active region filaments lie lower in the atmosphere than quiescent ones. The heights of the top dips range from  $\sim 1500$ – $5000$  km for the studied filaments. However, extrapolation runs with different grid resolutions in  $z$ -direction give different heights, which needs to be further studied. Also, we do not include the gravity of the filament plasma here. How much the gravity would affect the height of magnetic dips is still an open question. The answer needs more sophisticated modelling like nonlinear magneto-hydrostatic models (Wiegelmann & Neukirch 2006) or even full MHD simulations, as well as precise estimations of the plasma density within the filament.

The magnetic field strength in the rope center is  $\sim 700$  gauss, which is larger than findings in previous measurements or modelling of active region filaments by Wiehr & Stellmacher (1991), Aulanier & Démoulin (2003), and Sasso et al. (2007), where field strengths of 150, 40, and 380 gauss have been obtained, respectively. However, recently Kuckein et al. (2009) reported  $\sim 600$ – $700$  gauss for an active region filament, obtained from analyzing the full Stokes profiles in the He I  $D_3$  10830 Å spectral region. Our result is consistent with their values.

In summary, our magnetic field extrapolation permits to understand the complex shape and structure of the observed  $H\alpha$  filament. The good agreement between the locations of the magnetic dips and the filament is a further successful test of the method developed. About two hours after the time for which the presented extrapolation was obtained, an M1.1 class flare occurred. The magnetic flux rope is located at the place where the eruption was initiated. Our present results will be the base of further research to understand the initiation of this eruption.

THEMIS is a French-Italian telescope operated by the CNRS and CNR on the island of Tenerife in the Spanish Observatorio del Teide of the Instituto de Astrofísica de Canarias. Y. Guo was supported by the scholarship granted by China Scholarship Council (CSC) under file No. 2008619058, by NSFC under grants 10828306 and 10933003, and by NKBRFSF under grant 2006CB806302. Financial supports by the European Commission through the FP6 SOLAIRE Network (MTRN-CT- 2006-035484) and through the FP7 SOTERIA project (Grant Agreement no 218816) are gratefully acknowledged. T. Wiegmann was supported by DLR-grant 50 OC 453 0501.

## REFERENCES

- Aly, J. J. 1989, *Sol. Phys.*, 120, 19
- Antiochos, S. K., Dahlburg, R. B., & Klimchuk, J. A. 1994, *ApJ*, 420, L41
- Antiochos, S. K., DeVore, C. R., & Klimchuk, J. A. 1999, *ApJ*, 510, 485
- Aulanier, G. & Démoulin, P. 1998, *A&A*, 329, 1125
- . 2003, *A&A*, 402, 769
- Aulanier, G., Démoulin, P., Mein, N., van Driel-Gesztelyi, L., Mein, P., & Schmieder, B. 1999, *A&A*, 342, 867
- Aulanier, G., Démoulin, P., van Driel-Gesztelyi, L., Mein, P., & Deforest, C. 1998, *A&A*, 335, 309
- Aulanier, G., DeVore, C. R., & Antiochos, S. K. 2002, *ApJ*, 567, L97
- Bobra, M. G., van Ballegooijen, A. A., & DeLuca, E. E. 2008, *ApJ*, 672, 1209
- Bommier, V., Landi Degl’Innocenti, E., Landolfi, M., & Molodij, G. 2007, *A&A*, 464, 323
- Bommier, V. & Molodij, G. 2002, *A&A*, 381, 241
- Bommier, V. & Rayrole, J. 2002, *A&A*, 381, 227
- Canfield, R. C., de La Beaujardière, J.-F., Fan, Y., Leka, K. D., McClymont, A. N., Metcalf, T. R., Mickey, D. L., Wuelser, J.-P., & Lites, B. W. 1993, *ApJ*, 411, 362
- Canou, A., Amari, T., Bommier, V., Schmieder, B., Aulanier, G., & Li, H. 2009, *ApJ*, 693, L27

- Chandra, R., Pariat, E., Schmieder, B., Mandrini, C. H., & Uddin, W. 2010, *Sol. Phys.*, 261, 127
- Démoulin, P. 1998, in *Astronomical Society of the Pacific Conference Series*, Vol. 150, IAU Colloq. 167: *New Perspectives on Solar Prominences*, ed. D. F. Webb, B. Schmieder, & D. M. Rust, 78–85
- DeRosa, M. L., Schrijver, C. J., Barnes, G., Leka, K. D., Lites, B. W., Aschwanden, M. J., Amari, T., Canou, A., McTiernan, J. M., Régnier, S., Thalmann, J. K., Valori, G., Wheatland, M. S., Wiegmann, T., Cheung, M. C. M., Conlon, P. A., Fuhrmann, M., Inhester, B., & Tadesse, T. 2009, *ApJ*, 696, 1780
- Dudík, J., Aulanier, G., Schmieder, B., Bommier, V., & Roudier, T. 2008, *Sol. Phys.*, 248, 29
- Fan, Y. & Gibson, S. E. 2007, *ApJ*, 668, 1232
- Forbes, T. G. & Isenberg, P. A. 1991, *ApJ*, 373, 294
- Georgoulis, M. K. 2005, *ApJ*, 629, L69
- Guo, Y., Ding, M. D., Wiegmann, T., & Li, H. 2008, *ApJ*, 679, 1629
- Guo, Y., Schmieder, B., Bommier, V., & Gosain, S. 2010, *Sol. Phys.*, 262, 35
- Jing, J., Chen, P. F., Wiegmann, T., Xu, Y., Park, S., & Wang, H. 2009, *ApJ*, 696, 84
- Judge, P. G. 1998, *ApJ*, 500, 1009
- Kippenhahn, R. & Schlüter, A. 1957, *Zeitschrift für Astrophysik*, 43, 36
- Kuckein, C., Centeno, R., Martínez Pillet, V., Casini, R., Manso Sainz, R., & Shimizu, T. 2009, *A&A*, 501, 1113
- Kuperus, M. & Raadu, M. A. 1974, *A&A*, 31, 189
- Landolfi, M. & Landi Degl’Innocenti, E. 1982, *Sol. Phys.*, 78, 355
- Leka, K. D. & Skumanich, A. 1999, *Sol. Phys.*, 188, 3
- Lin, H., Penn, M. J., & Tomczyk, S. 2000, *ApJ*, 541, L83
- Lites, B. W. 2005, *ApJ*, 622, 1275
- Liu, Y. & Lin, H. 2008, *ApJ*, 680, 1496

- López Ariste, A., Aulanier, G., Schmieder, B., & Sainz Dalda, A. 2006, *A&A*, 456, 725
- López Ariste, A., Rayrole, J., & Semel, M. 2000, *A&AS*, 142, 137
- Low, B. C. & Lou, Y. Q. 1990, *ApJ*, 352, 343
- Low, B. C. & Zhang, M. 2004, *ApJ*, 609, 1098
- Mackay, D. H., Gaizauskas, V., & van Ballegooijen, A. A. 2000, *ApJ*, 544, 1122
- Mackay, D. H., Karpen, J., Ballester, J., Schmieder, B., & Aulanier, G. 2010, *Space Sci. Rev.*, accepted
- Mackay, D. H., Longbottom, A. W., & Priest, E. R. 1999, *Sol. Phys.*, 185, 87
- Mackay, D. H. & van Ballegooijen, A. A. 2006, *ApJ*, 641, 577
- . 2009, *Sol. Phys.*, 260, 321
- Martin, S. F. 1998, in *Astronomical Society of the Pacific Conference Series*, Vol. 150, IAU Colloq. 167: *New Perspectives on Solar Prominences*, ed. D. F. Webb, B. Schmieder, & D. M. Rust, 419
- Martin, S. F., Bilimoria, R., & Tracadas, P. W. 1994, in *Solar Surface Magnetism*, ed. R. J. Rutten & C. J. Schrijver, 303
- Metcalf, T. R., Derosa, M. L., Schrijver, C. J., Barnes, G., van Ballegooijen, A. A., Wiegmann, T., Wheatland, M. S., Valori, G., & McTiernan, J. M. 2008, *Sol. Phys.*, 247, 269
- Metcalf, T. R., Leka, K. D., Barnes, G., Lites, B. W., Georgoulis, M. K., Pevtsov, A. A., Balasubramaniam, K. S., Gary, G. A., Jing, J., Li, J., Liu, Y., Wang, H. N., Abramenko, V., Yurchyshyn, V., & Moon, Y.-J. 2006, *Sol. Phys.*, 237, 267
- Moore, R. L., Sterling, A. C., Hudson, H. S., & Lemen, J. R. 2001, *ApJ*, 552, 833
- Okamoto, T. J., Tsuneta, S., Lites, B. W., Kubo, M., Yokoyama, T., Berger, T. E., Ichimoto, K., Katsukawa, Y., Nagata, S., Shibata, K., Shimizu, T., Shine, R. A., Suematsu, Y., Tarbell, T. D., & Title, A. M. 2008, *ApJ*, 673, L215
- Pevtsov, A. A., Canfield, R. C., & Metcalf, T. R. 1995, *ApJ*, 440, L109
- Régnier, S. & Amari, T. 2004, *A&A*, 425, 345
- Régnier, S., Amari, T., & Kersalé, E. 2002, *A&A*, 392, 1119

- Sasso, C., Lagg, A., Solanki, S. K., Aznar Cuadrado, R., & Collados, M. 2007, in *Astronomical Society of the Pacific Conference Series*, Vol. 368, *The Physics of Chromospheric Plasmas*, ed. P. Heinzel, I. Dorotovič, & R. J. Rutten, 467
- Scherrer, P. H., Bogart, R. S., Bush, R. I., Hoeksema, J. T., Kosovichev, A. G., Schou, J., Rosenberg, W., Springer, L., Tarbell, T. D., Title, A., Wolfson, C. J., Zayer, I., & MDI Engineering Team. 1995, *Sol. Phys.*, 162, 129
- Schrijver, C. J., De Rosa, M. L., Title, A. M., & Metcalf, T. R. 2005, *ApJ*, 628, 501
- Schrijver, C. J., Derosa, M. L., Metcalf, T. R., Liu, Y., McTiernan, J., Régnier, S., Valori, G., Wheatland, M. S., & Wiegelmann, T. 2006, *Sol. Phys.*, 235, 161
- Skumanich, A. & Lites, B. W. 1987, *ApJ*, 322, 473
- Socas-Navarro, H. 2001, in *Astronomical Society of the Pacific Conference Series*, Vol. 236, *Advanced Solar Polarimetry – Theory, Observation, and Instrumentation*, ed. M. Sigwarth, 487
- Su, Y., van Ballegoijen, A., Schmieder, B., Berlicki, A., Guo, Y., Golub, L., & Huang, G. 2009, *ApJ*, 704, 341
- Tandberg-Hanssen, E. 1995, *The nature of solar prominences* (Dordrecht: Kluwer)
- Titov, V. S. & Démoulin, P. 1999, *A&A*, 351, 707
- Titov, V. S., Priest, E. R., & Démoulin, P. 1993, *A&A*, 276, 564
- Török, T. & Kliem, B. 2003, *A&A*, 406, 1043
- . 2005, *ApJ*, 630, L97
- Valori, G., Kliem, B., & Keppens, R. 2005, *A&A*, 433, 335
- Valori, G., Kliem, B., & Török, T. 2010, *A&A*, submitted
- van Ballegoijen, A. A. 2004, *ApJ*, 612, 519
- van Ballegoijen, A. A., Priest, E. R., & Mackay, D. H. 2000, *ApJ*, 539, 983
- Wang, H., Yan, Y., & Sakurai, T. 2001, *Sol. Phys.*, 201, 323
- Wheatland, M. S. & Régnier, S. 2009, *ApJ*, 700, L88
- Wheatland, M. S., Sturrock, P. A., & Roumeliotis, G. 2000, *ApJ*, 540, 1150

Wiegelmann, T. 2004, *Sol. Phys.*, 219, 87

—. 2008, *J. Geophys. Res.*, 113, A03S02

Wiegelmann, T., Inhester, B., Kliem, B., Valori, G., & Neukirch, T. 2006a, *A&A*, 453, 737

Wiegelmann, T., Inhester, B., & Sakurai, T. 2006b, *Sol. Phys.*, 233, 215

Wiegelmann, T. & Neukirch, T. 2006, *A&A*, 457, 1053

Wiehr, E. & Stellmacher, G. 1991, *A&A*, 247, 379

Yan, Y., Aschwanden, M. J., Wang, S., & Deng, Y. 2001a, *Sol. Phys.*, 204, 27

Yan, Y., Deng, Y., Karlický, M., Fu, Q., Wang, S., & Liu, Y. 2001b, *ApJ*, 551, L115

Table 1: Metrics for the NLFFF extrapolation with the optimization method.

Boundary <sup>1</sup>	$E/E_{\text{pot}}$ <sup>2</sup>	$\langle \text{CW} \sin \theta \rangle$ <sup>3</sup>	$\langle  f_i  \rangle$ <sup>4</sup>
WP	1.36	0.28	$4.9 \times 10^{-3}$
MP	1.10	0.47	$5.7 \times 10^{-3}$
NP	1.01	0.68	$5.1 \times 10^{-3}$

<sup>1</sup> WP: Wiegelmann’s preprocessing and smoothing on the observed FOV (Wiegelmann et al. 2006b); MP: Wiegelmann’s preprocessing and smoothing on the flux balanced FOV embedded in the MDI magnetogram; NP: no preprocessing, no smoothing and no embedding.

<sup>2</sup> Energy contained in the NLFFF divided by the potential field energy for the same  $B_z$  distribution at the photosphere. The energies are calculated in the selected volume shown in Figure 5.

<sup>3</sup> Current-weighted average of the sine of the angle between the electric current density and the magnetic field, as defined by Equations (2,3).

<sup>4</sup> The unsigned average of the fractional flux change  $|f_i| = |(\nabla \cdot \mathbf{B})_i| / (6B_i / \Delta x)$ , where  $\Delta x$  is the grid spacing of the cubic mesh. Both  $\langle \text{CW} \sin \theta \rangle$  and  $\langle |f_i| \rangle$  are averaged over all grid points in the selected volume shown in Figure 5.

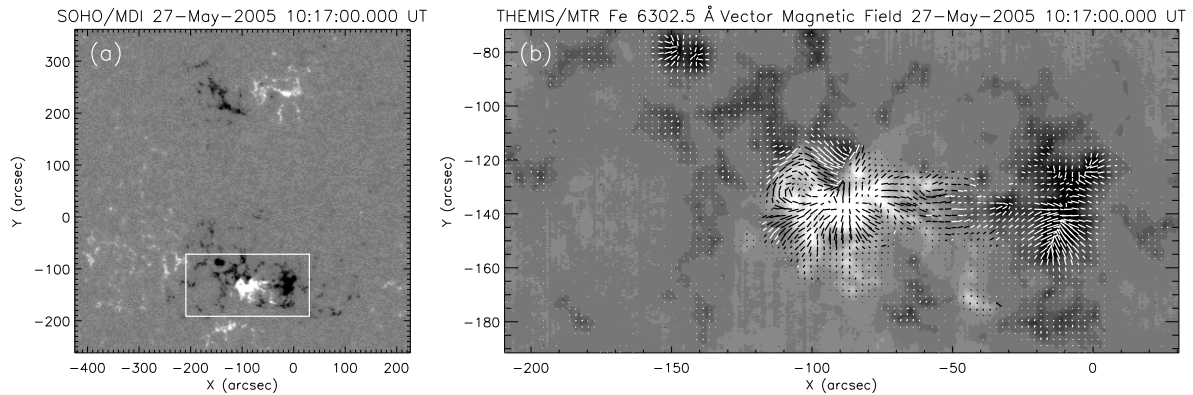


Fig. 1.— The magnetic fields for active region NOAA 10767 on 2005 May 27. (a) Part of the full disk magnetogram observed by SOHO/MDI. White/black corresponds to positive/negative polarity. The solid rectangle denotes the full FOV of THEMIS/MTR; (b) The vector magnetic fields observed by THEMIS/MTR in the Fe 6302.5 Å spectral line. The 180° ambiguity of the transverse fields is not removed, so that only arrows without arrow heads are used to represent the transverse fields.

Table 2: Comparison of patterns and magnetic structures of the filament with a theoretical model.

	Eastern part	Western part	Wire model <sup>1</sup>
Axial field chirality <sup>2</sup>	Dextral	Dextral	Dextral
Filament barb chirality <sup>3</sup>	Right-bearing	Left-bearing	Right-bearing
Magnetic field configuration	Flux rope	Arcade <sup>4</sup>	Arcade <sup>4</sup>
Magnetic field geometry	Dip	Dip	Flat
Magnetic field orientation	Inverse	Normal	Inverse
Filament field helicity sign	$< 0$	$< 0$	$> 0$
Overlying arcade helicity sign	$< 0$	$< 0$	$< 0$

<sup>1</sup> Referred to Martin et al. (1994) and Martin (1998).

<sup>2</sup> The chirality of axial magnetic field is defined as follows. Sitting and viewing a filament from the main positive magnetic polarity, if its axial magnetic field component points to the right/left, the filament is dextral/sinistral.

<sup>3</sup> The chirality of filament barbs is defined as follows. Viewed from either side of a filament, if the barbs on the side closer to the observer veer from the filament axis to the right/left, the filament is right-bearing/left-bearing.

<sup>4</sup> The arcade in our studied filament includes the quadrupolar FBP/FX arcade ( $x \in [-70, -50]$  arcsec, Figure 6f) and the bipolar sheared arcade with normal polarity ( $x \in [-90, -70]$  arcsec, Figure 6f). Both arcades are rooted in the main polarities. An arcade in the wire model is rooted in the parasitic polarities.

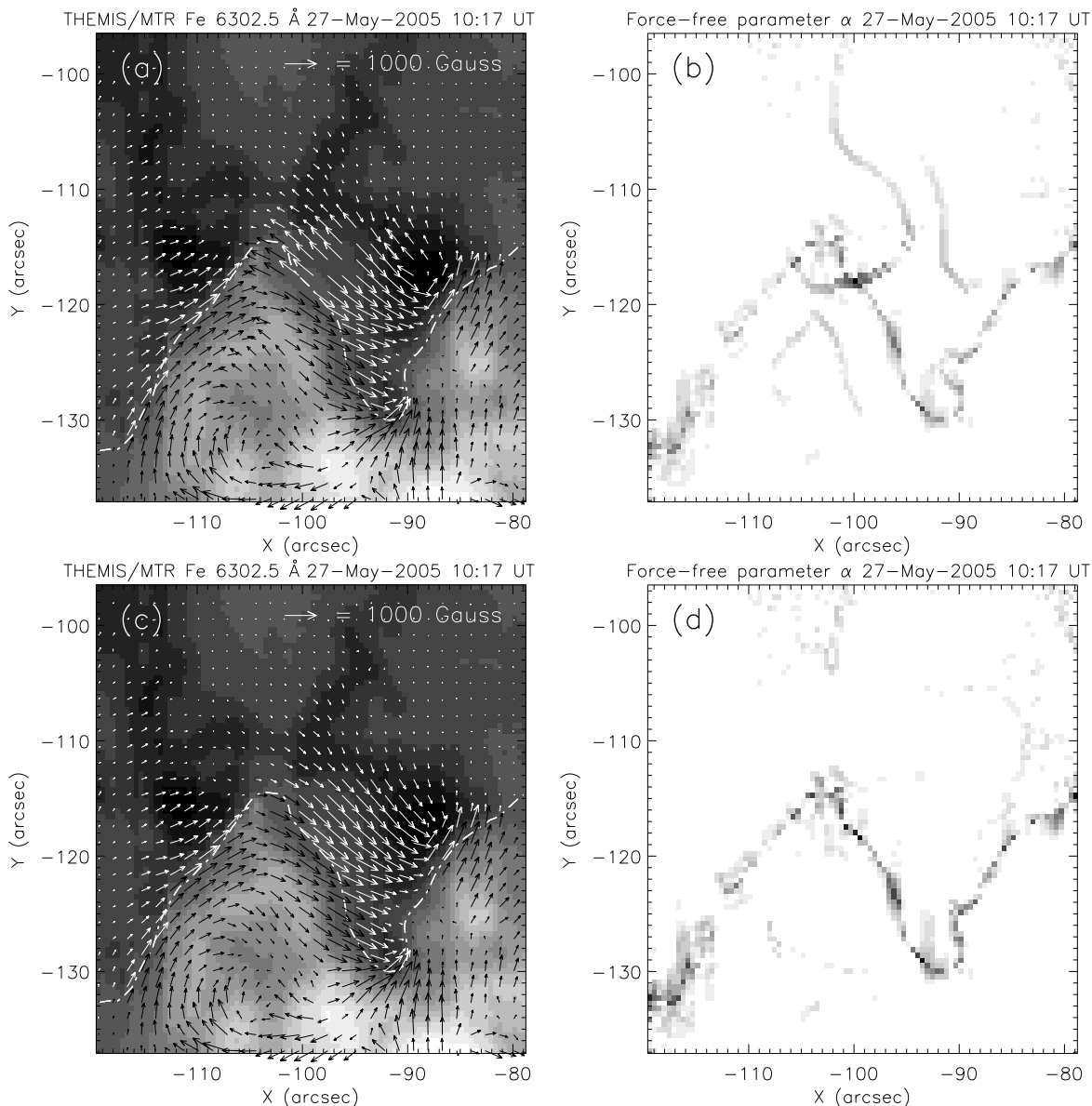


Fig. 2.— The vector magnetic fields and the absolute value of the force-free parameter  $\alpha$  in a sub-region of the THEMIS/MTR FOV after removing the  $180^\circ$  ambiguity. (a,b) Using the non-potential magnetic field calculation method; (c,d) Removing the ambiguity by additionally flipping the transverse fields of panel (a) in the region enclosed by large line-of-sight currents (see Figure 3 and text for details). The transverse and line-of-sight fields are represented by arrows and gray levels, respectively.

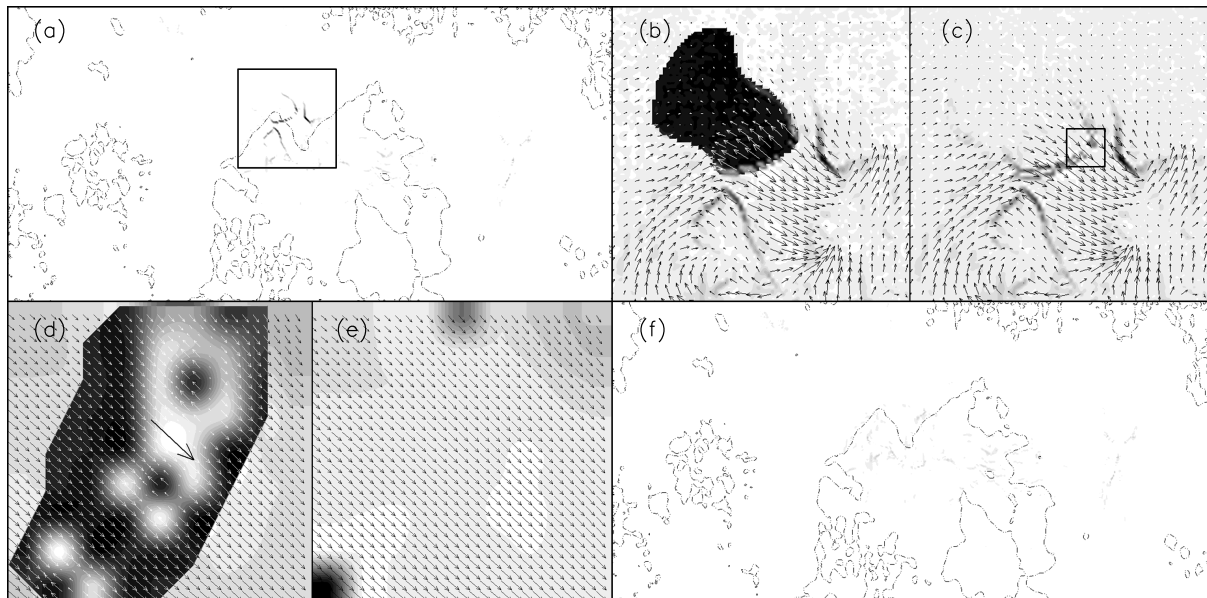


Fig. 3.— The absolute value of the line-of-sight current  $|J_z|$  (gray levels) and the transverse magnetic fields (arrows) in the process of removing the  $180^\circ$  ambiguity. (a) The dashed contour represents the inversion line of the line-of-sight magnetic field  $B_z$ . The solid rectangle denotes the FOV of panels (b,c).  $|J_z|$  is larger in darker regions of the gray scale image; (b) The dark (gray-scale reversed) region is selected to flip the transverse fields; (c) The transverse fields in the dark region have been flipped. The solid rectangle marks the FOV of panels (d,e); (d) The dark region is selected, where the transverse field will be flipped if it makes an obtuse angle with the defined direction denoted by the larger arrow. The white regions inside the dark (gray-scale reversed) region show the strongest  $|J_z|$ ; (e) The transverse field in the selected region has been changed; (f)  $|J_z|$  after removing the  $180^\circ$  ambiguity by repeating the operations shown in (b–e).

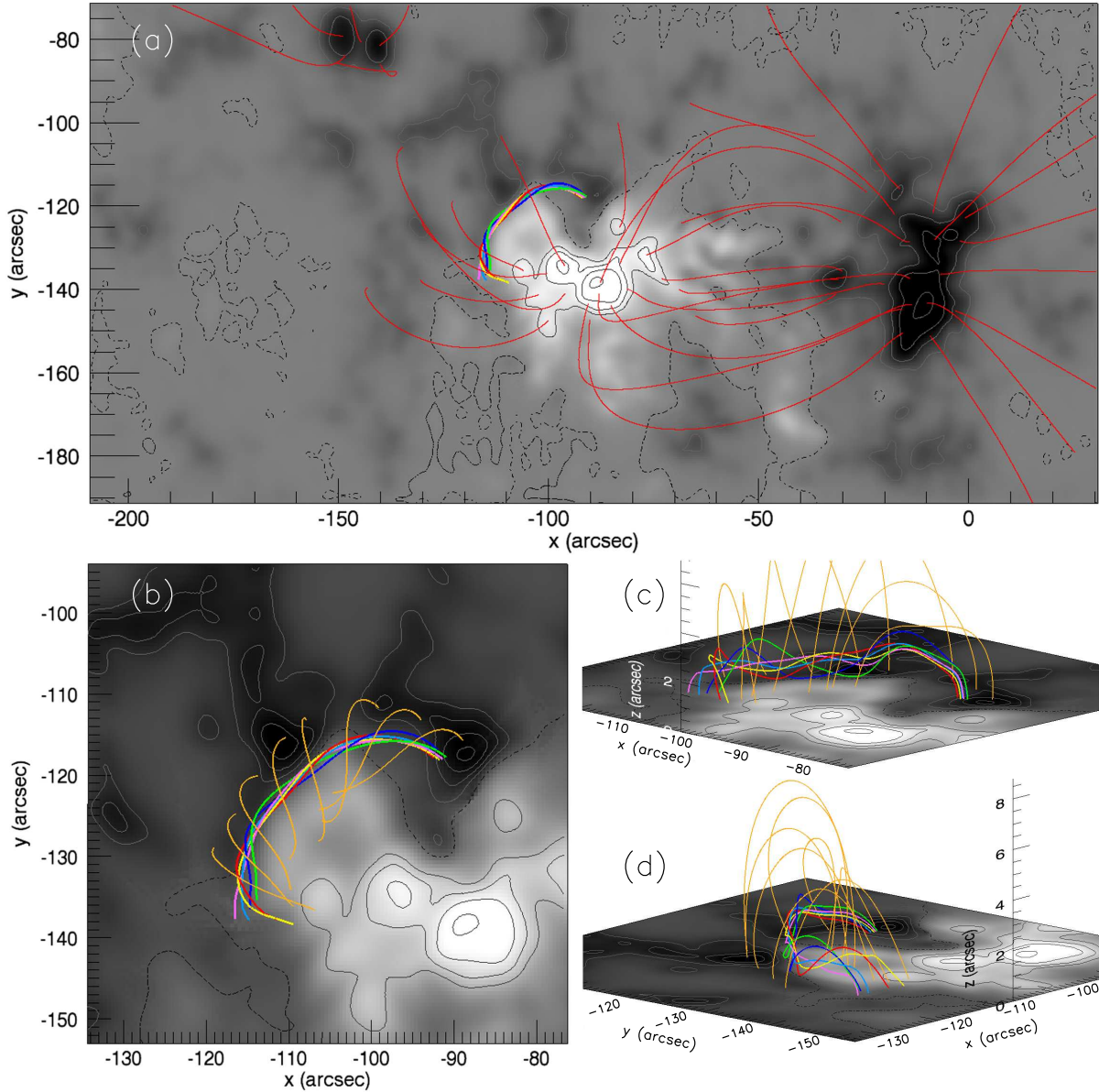


Fig. 4.— Selected magnetic field lines of the active region (red) and the flux rope (mixed colors). (a) Top view on the whole observed region. The line-of-sight magnetic field  $B_z$  is displayed by both the gray-scale image and contours. White (black) image stands for  $B_z > 0$  ( $B_z < 0$ ); (b) Top view on the magnetic flux rope. Different colors are used to outline the twist of the field lines. Red, dark blue, and green field lines are calculated by integrating from three selected points slightly above the inversion line into both directions. Orange field lines are selected close to the magnetic flux rope; (c,d) Side views on the magnetic flux rope. The vertical scale is enlarged by a factor of 3.

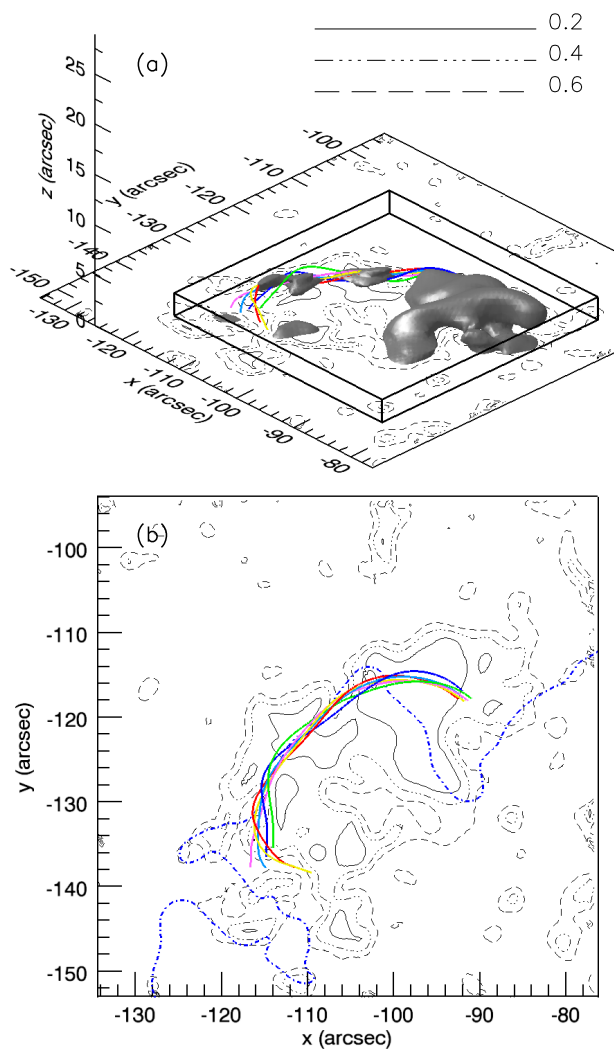


Fig. 5.— (a) The contours show the sine of the angle between the magnetic field and the current density at the bottom layer (Equation 3). The iso-surface marks locations with 40% of the peak of the electric current density in this volume. The rectangular box is selected to calculate the metrics measuring the force-free and divergence-free state of the modelled magnetic field (see text and Table 1 for details). The colored field lines of the flux rope are the same as in Figure 4; (b) As panel (a), but without the iso-surface and viewed from above. The blue dash-dotted line represents the polarity inversion line of  $B_z$ .

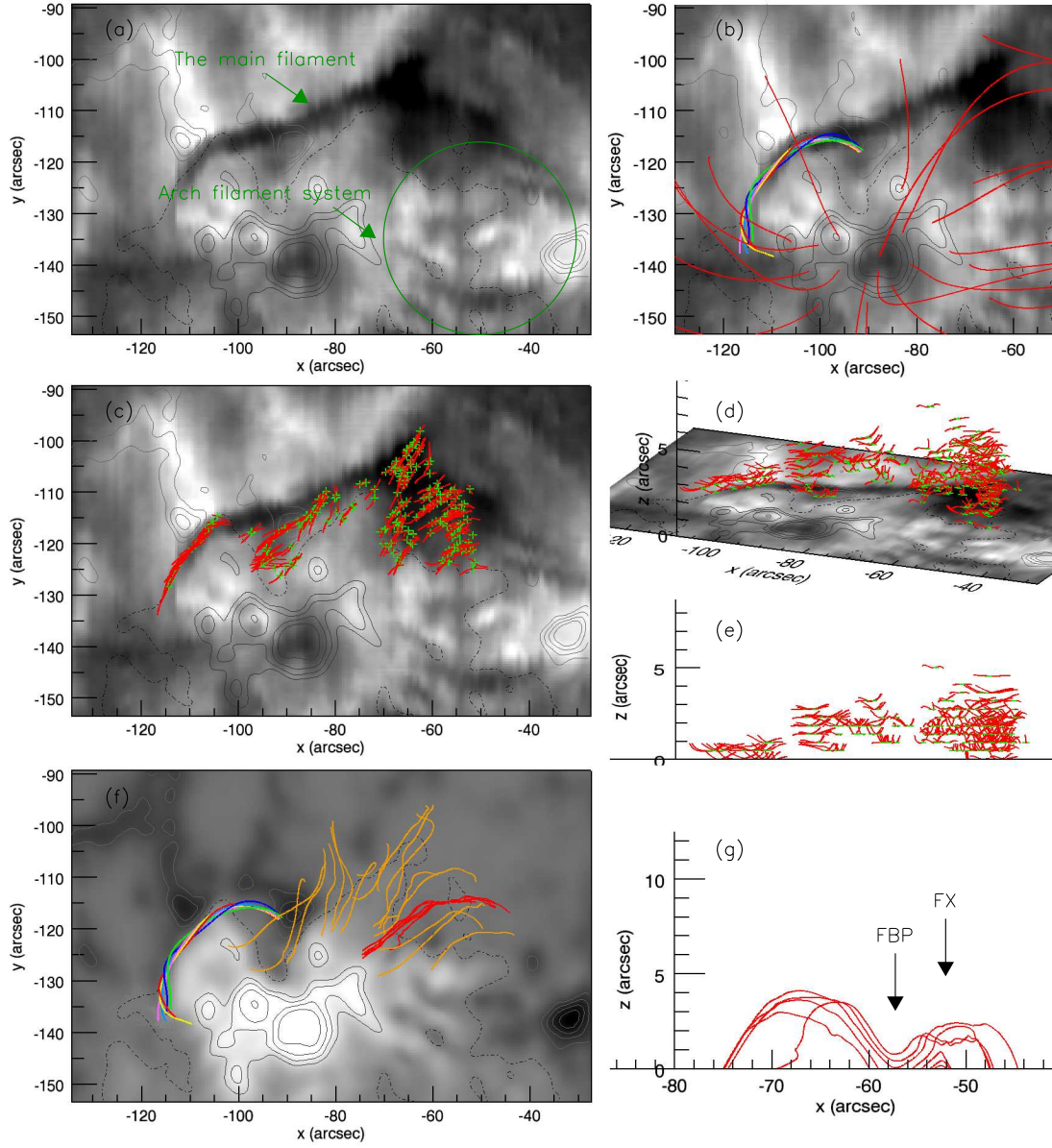


Fig. 6.— (a) The filament observed in the H $\alpha$  line center by THEMIS/MTR; (b) Overlay of the H $\alpha$  image and the extrapolated magnetic field. The colored field lines are the same as in Figure 4; (c–e) Dips (green ‘+’ signs) found in the extrapolated magnetic field (calculated with a grid spacing of  $\sim 330$  km in the vertical direction). The red field lines starting from the dipoles are integrated in both directions up to a filling height of 300 km, or to a local maximum if they start to descend before that height. Different panels show different viewing angles. The contours represent the line-of-sight magnetic field  $B_z$ ; (f) The orange field lines start from selected dipoles and are integrated until they go out of the box. The red field lines in the western part are integrated from randomly distributed sample points on the section at  $x \in [-60.0, -50.0]$  arcsec,  $y = -114.7$  arcsec, and  $z \in [0.0, 1.0]$  arcsec. The gray-scale image shows the line-of-sight magnetic field  $B_z$ ; (g) Edge-on view on the red field lines shown in Figure 6f.

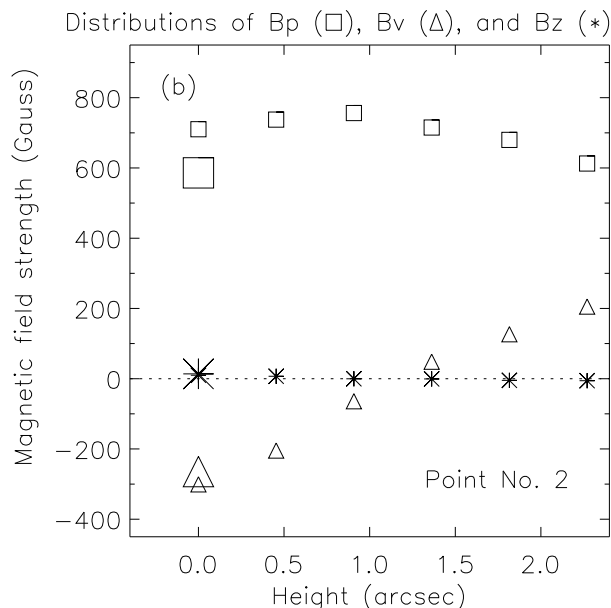
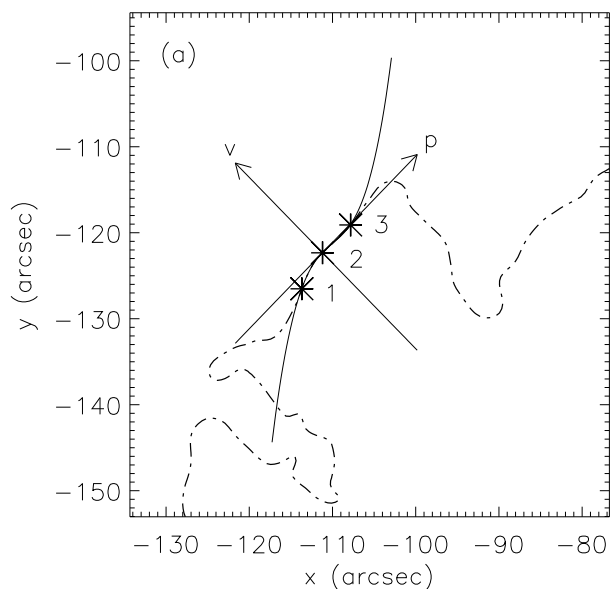


Fig. 7.— (a) The local coordinate system of the flux rope. The dash-dotted line marks the polarity inversion line. In order to approximate the horizontal orientation of the flux rope axis, a third-order polynomial is fitted between points 1 and 3 to the inversion line. The central point 2 is then selected and the  $p$ - and  $v$ -direction are defined as tangential and normal directions, respectively; (b) The distributions of  $B_p$ ,  $B_v$  (the horizontal magnetic field components in the local coordinate system), and  $B_z$  along the  $z$ -direction at point 2. Square, triangle, and asterisk symbols denote  $B_p$ ,  $B_v$ , and  $B_z$ , respectively. The larger symbols at  $z = 0$  represent the original data before preprocessing. The smaller symbols are the preprocessed and extrapolated data.